

Supporting Information

High Oxygen Reduction Reaction Performances of Cathode Materials Combining Polyoxometalates, Coordination Complexes and Carbonaceous Supports

Shuangshuang Zhang,^{†, ⊥} Olivier Oms,[‡] Long Hao,^{//} Rongji Liu,[†] Meng Wang,[†] Yaqin Zhang,[†] Hong-Yan He,^{,†} Anne Dolbecq,[‡] Jérôme Marrot,[‡] Bineta Keita,^{\$, ∇} Linjie Zhi,^{//} Pierre Mialane,^{*,‡} Bin Li ^{//} and Guangjin Zhang^{*,†}*

[†] Key Laboratory of Green Process and Engineering, Institute of Process Engineering, Chinese Academy of Sciences, 100190, Beijing, China.

E-mail: hyhe@ipe.ac.cn.

E-mail: zhanggj@ipe.ac.cn.

[‡] Institut Lavoisier de Versailles, UMR 8180, Université Paris-Saclay, Université de Versailles Saint-Quentin en Yvelines, 45 Avenue des Etats-Unis, 78035 Versailles cedex (France). E-mail: pierre.mialane@uvsq.fr.

^{\$} Laboratoire de Chimie-Physique, UMR 8000 CNRS, Université Paris-Sud Orsay, F-91405, France.

“Key Laboratory of Nanosystem and Hierarchical Fabrication National Center for Nanoscience and Technology , 100190, Beijing, China.

” Zhengzhou Tobacco Research Institute of CNTC, 450001, Zhengzhou, China.

[⊥] College of Chemistry, Chemical Engineering and Materials Science, Collaborative Innovation Center of Functionalized Probes for Chemical Imaging in Universities of Shandong, Key Laboratory of Molecular and Nano Probes, Ministry of Education, Institute of Molecular and Nano Science, Shandong Normal University, Jinan 250014, P. R. China.

▽Retired

Experimental Details:

Synthesis and characterizations of the materials

TTF-400, TTF-700 and TTF-F used in this work were synthesized according to the published procedures.¹ Carbon Vulcan XC-72 were used directly as they were purchased. rGO were synthesized according to the published procedures.²

Synthesis of TTF-400 and TTF-700: Terephthalonitrile (1 g, 7.8 mmol) and anhydrous zinc chloride (5.32 g, 39 mmol) were mixed in a glove box (argon with 0.1 ppm oxygen and 0.1 ppm water) and transferred into a quartz ampoule (\varnothing 17 \times 180 mm), sealed and heated for 40 h at 400 °C for TTF-400 and 700 °C for TTF-700. Then the ampoule was cooled to room temperature and opened. The black solid was washed thoroughly with 5% HCl solution, deionized water and then dried under vacuum at 120 °C for 12 h to afford TTF-400 and TTF-700.

Synthesis of TTF-F: TTF-700 (100 mg) and ammonium fluoride (2 g) were mixed in a beaker containing 20 mL of deionized water and sonicated for 2 h. Then, the black solid was collected by centrifugation, dried under vacuum at 40 °C for 12 h, transferred into a quartz boat, heated at 600 °C under argon atmosphere for 2 h and then cooled down to room temperature to obtain TTF-F.

Synthesis of rGO: 1.2 g of glucose was added to 150 mL of a homogeneous GO dispersion in deionized water (0.5 mg/mL) and stirred for 30 min. Then, 590 μ L of an ammonia solution (25~28% w/w) was added to the resulting dispersion. After vigorously shaking for 15 min, the mixture was stirred for 90 min at 95 °C. The resulting black dispersion was then filtered, washed several times with water and the obtained rGO was redispersed in water for further use.^[2]

Synthesis of Cu₆Ni₇/C and Cu₆Ni₇/rGO: The POM (1 mg) and the C/rGO (1 mg) in ethanol (265μL) were grinded first for 10 min in a little glass bowl and then sonicated for at least 30 min to form a homogeneous ink. The obtained ink was heated at 60 °C under vacuum for one night and then cooled down to room temperature to obtain the desired composite.

Infrared Spectra were recorded on a Nicolet 6700 FT spectrometer. Elemental analyses were performed by the Service Central d'Analyse of CNRS, 69390 Vernaison, France (heavy elements) and by the Service de Microanalyse of CNRS, ICSN, 91198 Gif-sur-Yvette, France (C, H, N). For Cu₃P₂W₁₈, the tungsten/copper, tungsten/phosphor and copper/phosphor ratios were evaluated using a Jeol JSM-5800LV Scanning Microscope equipped with an integrated EDX system.

X-ray Diffraction. Intensity data collection was carried out with a Bruker D8 VENTURE diffractometer equipped with a PHOTON 100 CMOS bidimensional detector using a high brilliance IμS microfocus X-ray Mo Kα monochromatized radiation ($\lambda = 0.71073 \text{ \AA}$). The absorption corrections were based on multiple and symmetry-equivalent reflections in the data sets using the SADABS program^[3] based on the method of Blessing.^[4] The structures were solved by direct methods and refined by full-matrix least-squares using the SHELX-TL package.^[5] The hydrogen atoms were theoretically located on the basis of the conformation of the supporting atoms.

XPS measurements were carried out on an ESCALAB250Xi apparatus at base pressure of 1×10^{-9} mbar, and X-ray source of Al Kα. TEM images were got from a JEM-2100 (UHL) transmission electron microscope at an acceleration voltage of 200kV. The FESEM and elemental mapping images were performed on a SU8020 field emission scanning electron microscope. The Raman spectra were obtained with a Renishaw Raman System Model 1000

spectrometer. The 532 nm radiation from a 20mW air-cooled argon ion laser was used as the exciting source. The laser diameter was 1 μ m and the laser power at the sample position was 4.0 mW. Powder XRD studies were recorded on an Empyrean (Holland PANalytical B.V.) advance powder diffractometer using a Cu K α 1 monochromatized radiation (λ = 1.54056 Å). Nitrogen sorption/desorption isotherms were measured at 77 K with an ASAP 2020 physisorption analyzer. The Brunauer-Emmett-Teller (BET) method and density functional theory (DFT) pore model were utilized to calculate the specific surface area (SSA) and pore size distribution, respectively.

Conductivity measurements: The electrochemical impedance spectra (EIS) were obtained from a ZAHNER ZENNIUM electrochemical workstation (ZAHNER Instrument Inc., Germany) in the presence of a 1 mM K₃[Fe(CN)₆]/K₄[Fe(CN)₆] (1:1, mol/mol) mixture as a redox probe in 0.1 M KCl aqueous solution. The frequency range was 100 000~0.01Hz with a signal amplitude of 5 mV.

Table S1. X-Ray crystallographic data of **Cu₆Ni₇**.

	Cu₆Ni₇
Formula	Cu ₆ W ₁₈ Ni ₇ P ₆ O ₁₂₈ C ₃₂ N ₂₄ H ₁₆₆ Na ₂
Fw [g]	7269
Crystal system	Monoclinic
Space group	<i>P2₁/n</i>
<i>Z</i>	2
<i>T</i> [K]	293(2)
<i>a</i> [Å]	18.059(2)
<i>b</i> [Å]	18.738(1)
<i>c</i> [Å]	19.951(2)
α [°]	90
β [°]	97.174(3)
γ [°]	90
<i>V</i> [Å ³]	6698.7(7)
ρ_{calc} [g cm ⁻³]	3.637
μ [mm ⁻¹]	17.488
Reflections collected	97415
Unique reflections (<i>R</i> _{int})	11954 (0.0707)
Refined parameters	818
GOF	1.175
<i>R</i> (<i>F</i> _o) ^a <i>I</i> > 2σ(<i>I</i>) (all data)	0.0561 (0.0773)
<i>R</i> _w (<i>F</i> _o ²) ^b	0.1474 (0.1607)

Oxygen Reduction Reaction (ORR) Measurements

CV measurements: POM (1 mg) and TTFs/rGO/C (1 mg) in ethanol (265.4 μL) were grinded first for 10min in a little glass bowl and then sonicated for at least 30 min to form a homogeneous ink. To prepare the working electrode for electrochemical measurements, 5 μL of this catalyst ink was loaded onto a mirror-polished glassy-carbon electrode of diameter 4 mm, giving a POM loading of 0.3 mg cm^{-2} . Following evaporation of the solvent in air, a thin layer of 0.5% Nafion solution was coated onto the electrode surface and then dried in air for 1 h to afford the working electrode. For comparison, a GCE coated with Pt/C (20 wt.% Pt on Vulcan XC-72, purchased from Alfa Aesar) was also fabricated according to the same process. The electrolytes were first saturated by bubbling O_2 through them prior to the measurements for at least 30 min. During the recording of CVs, a flow of O_2 was maintained over the electrolyte to ensure its continued O_2 saturation. In control experiments, CV measurements were performed in Ar-saturated electrolyte. The working electrode was cycled at least 10 times before data were recorded at a scan rate of 10 mV s^{-1} .

RDE measurements: For the RDE measurements, catalyst inks were prepared according to the same method as for CV measurements. The working electrode was scanned at rate of 10 mV s^{-1} with varying rotation speeds from 400 rpm to 1600 rpm. Koutecky–Levich plots (J^{-1} vs $\omega^{-1/2}$) were analyzed at various electrode potentials. The slopes of the linear plots were used to calculate the number of electrons transferred (n) on the basis of the following Koutecky–Levich equation [Eqs.(1) and (2)], in which J is the measured current density, J_K and J_L are the kinetic- and diffusion-limiting current densities, ω is the angular velocity, $F=96485 \text{ C mol}^{-1}$ is the Faraday constant, C_{O_2} ($0.938 \times 10^{-3} \text{ M}$ for neutral medium, $1.2 \times 10^{-3} \text{ M}$ for basic medium) is the bulk concentration of O_2 , D_{O_2} ($2.17 \times 10^{-5} \text{ cm}^2 \text{ s}^{-1}$ for neutral medium, $1.9 \times 10^{-5} \text{ cm}^2 \text{ s}^{-1}$ for basic

medium) is the O₂ diffusion coefficient, and ν (0.00956 cm² s⁻¹ for neutral medium, 0.01 cm² s⁻¹ for basic medium) is the kinematic viscosity of the electrolyte. The constant 0.2 is adopted when the rotating speed is expressed in rpm.

$$\frac{1}{J} = \frac{1}{J_L} + \frac{1}{J_K} = \frac{1}{B\omega^{1/2}} + \frac{1}{J_K}$$

$$B = 0.2nFC_{O_2}(D_{O_2})^{2/3}\nu^{-1/6}$$

Rotating ring-disk electrode (RRDE) measurements: For RRDE measurements, electrodes were prepared by the same method as for the CVs. The working electrode was scanned at a rate of 10 mVs⁻¹ with a rotation speed of 1600 rpm. The ring was held at +1.250 V vs. RHE (for basic media, the potential was 1.49 V vs. RHE). The % HO₂⁻ and the electron transfer number (n) were determined by the Equations (3) and (4), in which I_d is the disk current, I_r is the ring current, and N is the current collection efficiency of the Pt ring. In our system, N was determined as 0.43 from the reduction of K₃[Fe(CN)₆].

$$\%HO_2^- = 200 \times \frac{I_r/N}{I_d + I_r/N}$$

$$n = 4 \times \frac{I_d}{I_r/N}$$

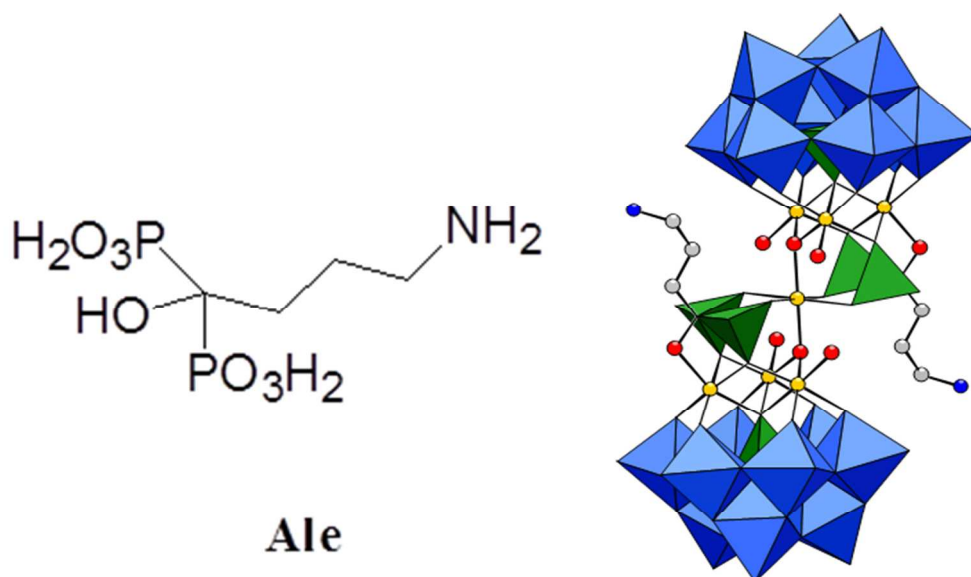


Figure S1. (left) The alendronate ligand; (right) the $\{(PW_9)_2M_7(Ale)_2\}$ ($M = Co^{II}, Ni^{II}$) core found in NH_4Co_7 , NH_4Ni_7 , $NaNH_4Co_7$, $NaKNi_7$, Cu_6Co_7 and Cu_6Ni_7 . Light blue octahedra, WO_6 ; yellow spheres, M; green tetrahedra, PO_4 or PO_3C ; grey spheres, C; blue spheres, N; red spheres, O; hydrogen atoms have been omitted for clarity.

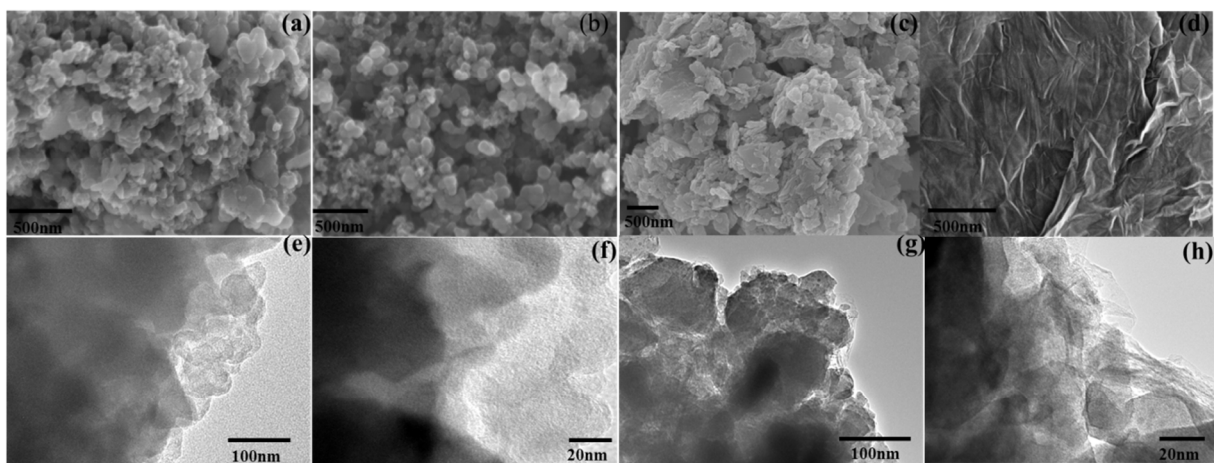


Figure S2. SEM images of (a) Cu_6Ni_7/C , (b) C, (c) Cu_6Ni_7/rGO , (d) rGO; TEM images of (e-f) Cu_6Ni_7/C , (g-h) Cu_6Ni_7/rGO .

SEM images clearly revealed the morphological and structural changes after the synthetic process (Figures S2). It could be observed that the carbon Vulcan XC-72 consisted of spherical nanostructures with an average diameter of 30–40 nm (Figure S2b). From figure S2d, we can also clearly observe that large scale rGO sheets with many crumpled silk veil waves were successfully obtained. For $\text{Cu}_6\text{Ni}_7/\text{C}$ and $\text{Cu}_6\text{Ni}_7/\text{rGO}$ (Figures S2a and S2c), we found that Cu_6Ni_7 were tightly attached on the surface of the C or rGO, forming a denser structure due to the strong interaction between them. Meanwhile, typical TEM (Figures S2e and 2g) and HRTEM (Figures S2f and 2h) images illustrate that many nanoclusters are dispersed on C or rGO.

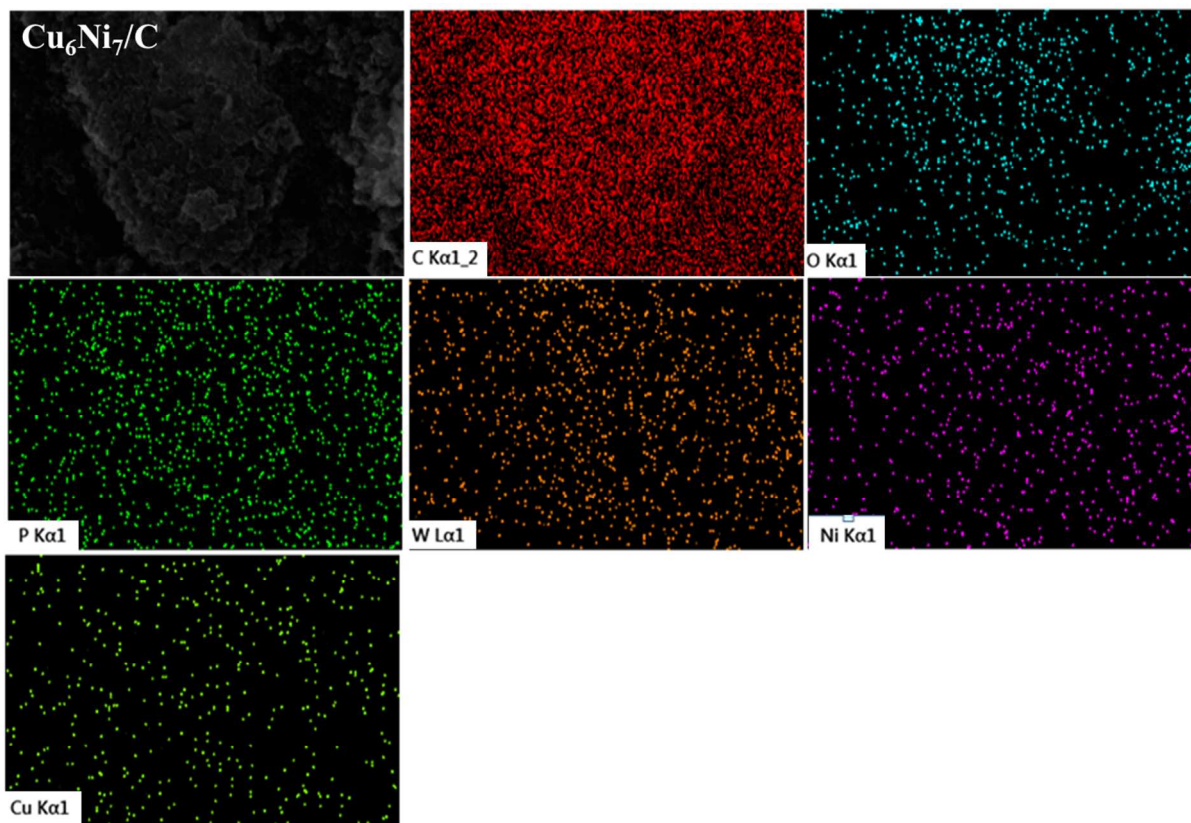


Figure S3. EDS elemental mapping images of $\text{Cu}_6\text{Ni}_7/\text{C}$.

The energy-dispersive X-ray spectrum (EDS) elemental mapping images (Figure S3) on C, O, P, W, Ni and Cu demonstrate the homogeneous distribution of Cu_6Ni_7 on the surface of C.

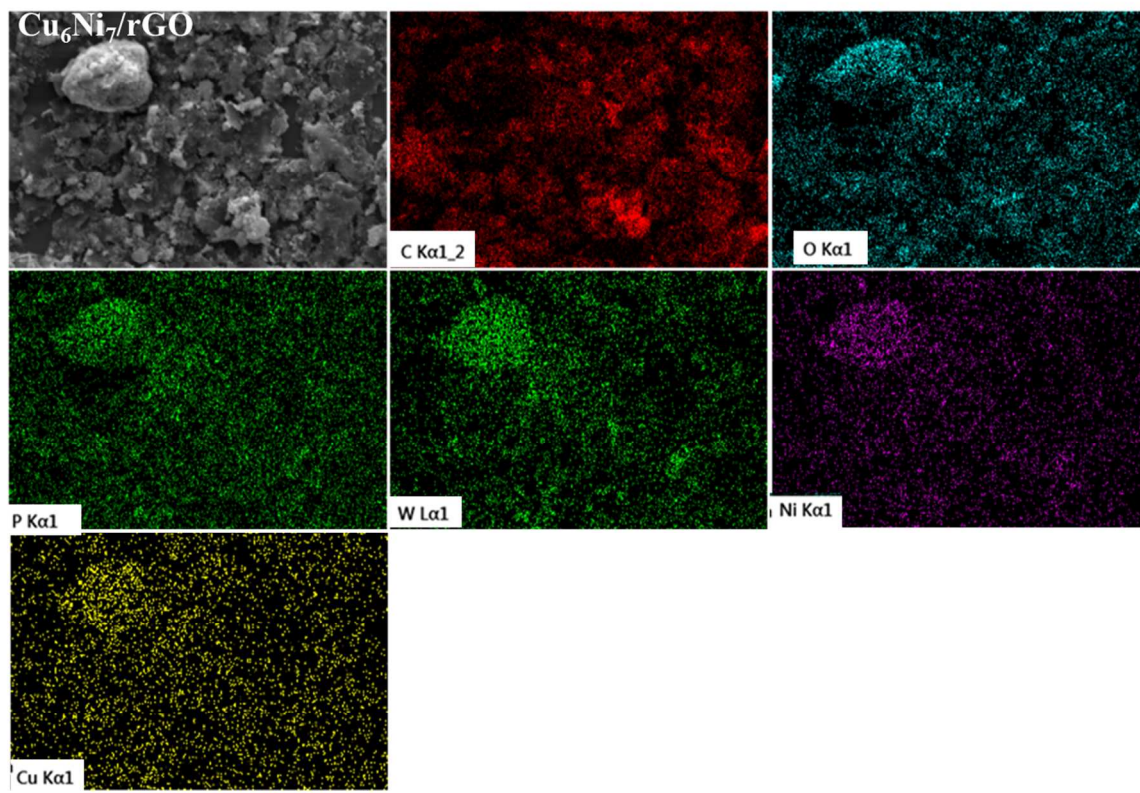


Figure S4. EDS elemental mapping images of $\text{Cu}_6\text{Ni}_7/\text{rGO}$.

The EDS elemental mapping images (Figure S4) on C, O, P, W, Ni and Cu also demonstrate the homogeneous distribution of Cu_6Ni_7 on the surface of rGO.

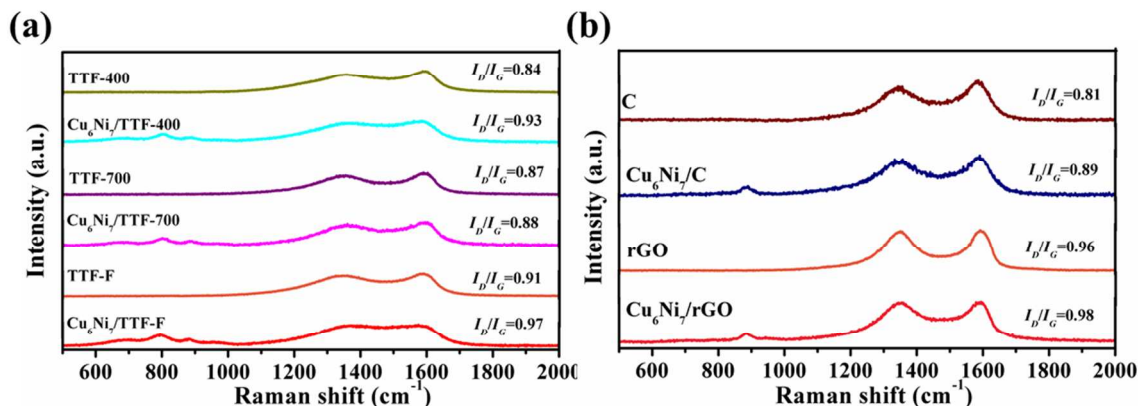


Figure S5. Raman spectra of (a) TTFs and $\text{Cu}_6\text{Ni}_7/\text{TTFs}$, (b) C and $\text{Cu}_6\text{Ni}_7/\text{C}$, rGO and $\text{Cu}_6\text{Ni}_7/\text{rGO}$.

Raman spectroscopy analyses show that all the spectra exhibit D and G bands at around 1350 and 1594 cm^{-1} , which are assigned to disordered sp^3 carbon and graphitic sp^2 carbon, respectively. It can be observed that pure C and rGO show a relatively weaker D-band compared to the composites, the values of I_D/I_G increasing with the introduction of Cu_6Ni_7 . This modification of resonance conditions upon functionalisation confirms the interaction of the supports with the POM molecules.

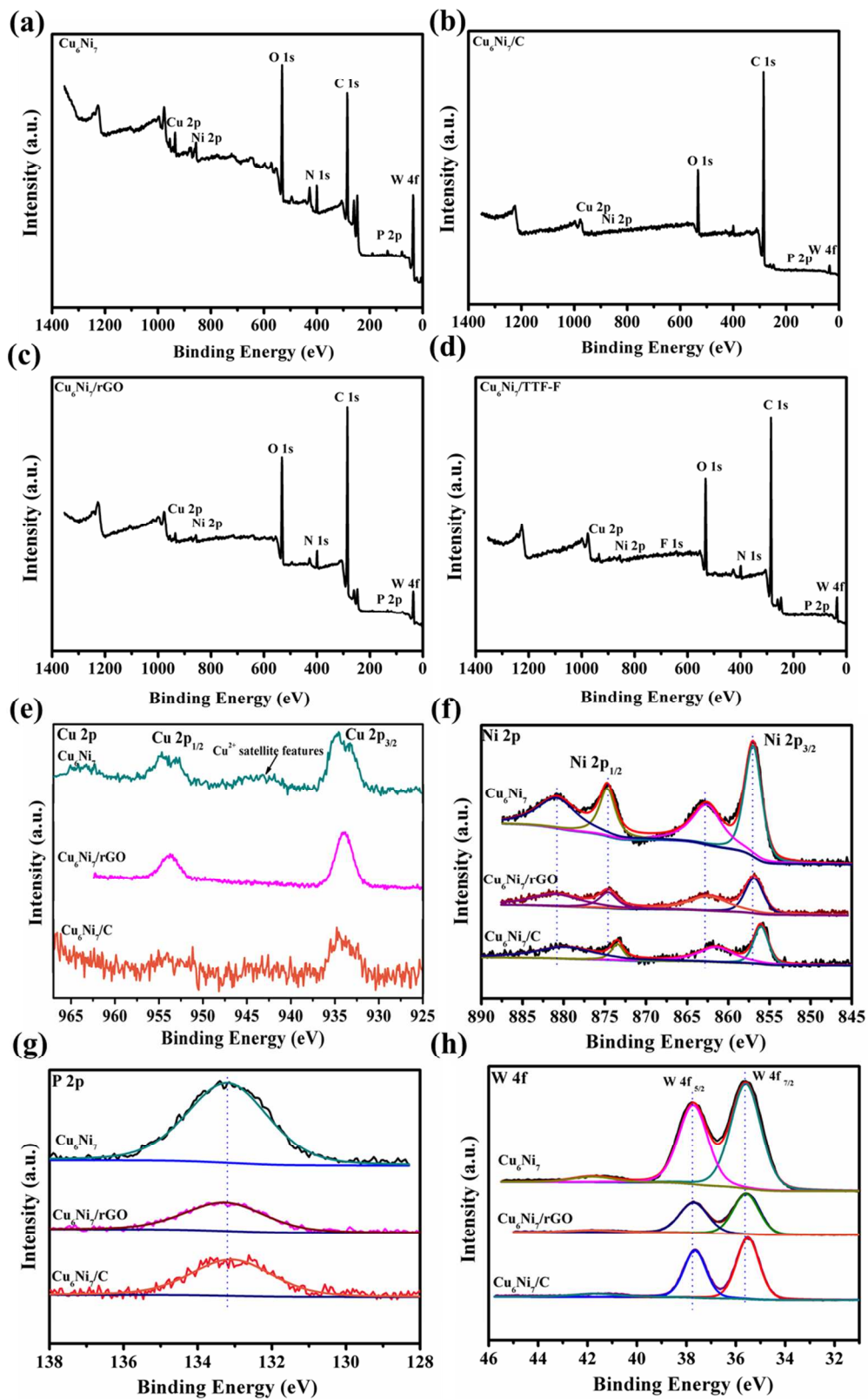
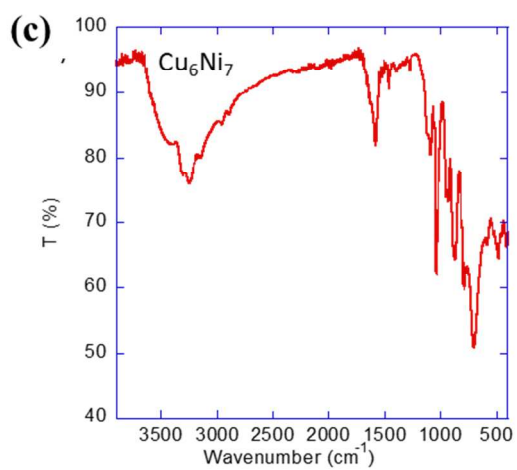
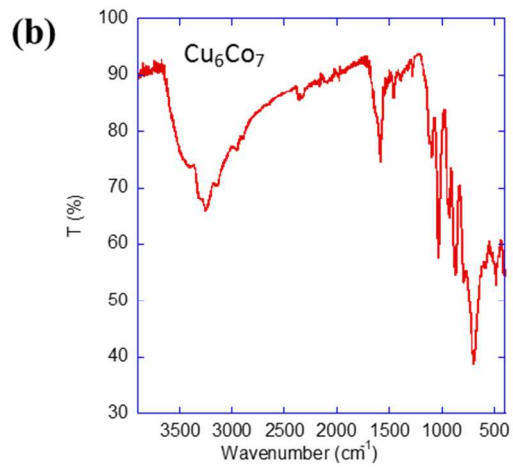
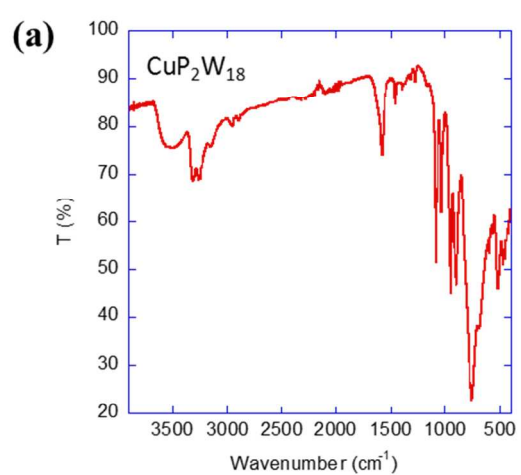


Figure S6. XPS spectra of Cu₆Ni₇ (a), Cu₆Ni₇/C (b), Cu₆Ni₇/rGO (c), Cu₆Ni₇/TTF-F (d), Cu 2P, Ni 2p, P 2P and W 4f spectrum of Cu₆Ni₇, Cu₆Ni₇/rGO and Cu₆Ni₇/C (e-h).

For Cu₆Ni₇/C and Cu₆Ni₇/rGO, their XPS survey spectra show Cu, Ni, P and W signals, in contrast to those of C/rGO, and in line with the presence of Cu₆Ni₇ POMs (Figure S6 a-c). To be specific, the XPS peaks of Cu element at ~951-957 and ~930-938 eV are assigned to Cu 2p_{1/2} and Cu 2p_{3/2} respectively (Figure S6e). A relative weak Cu^{II} satellite peaks at ~940–947 and ~958–965 eV were also noted. The Ni 2p XPS spectrum could be deconvoluted into one spin-orbit coupling and two shake-up satellites located at ~862.8 eV and ~880.8 eV. The doublet with binding energy at ~856.2 eV (Ni 2p_{3/2}) and 873.8 eV (Ni 2p_{1/2}) showing energy difference gap of 17.6 eV was assigned to Ni^{II} phase (Figure S6f). The presence of P was also detected in the hybrids as shown in Figure S6g. For W, there are W 4f_{5/2} and W 4f_{7/2} doublet with the binding energies of ~37.7 and ~35.6 eV, respectively (Figure S6h), confirming that the tungsten atoms are in their full oxidation states in the deposited Cu₆Ni₇. Importantly, it should be noted that all of the P 2p, W 4f, Cu 2p, and Ni 2p peaks of Cu₆Ni₇/C and Cu₆Ni₇/rGO are shifted to lower binding energies compared with those of pure Cu₆Ni₇. This suggests electron transfer from Cu₆Ni₇ to C or rGO and confirms the strong interaction between the POM and the support.



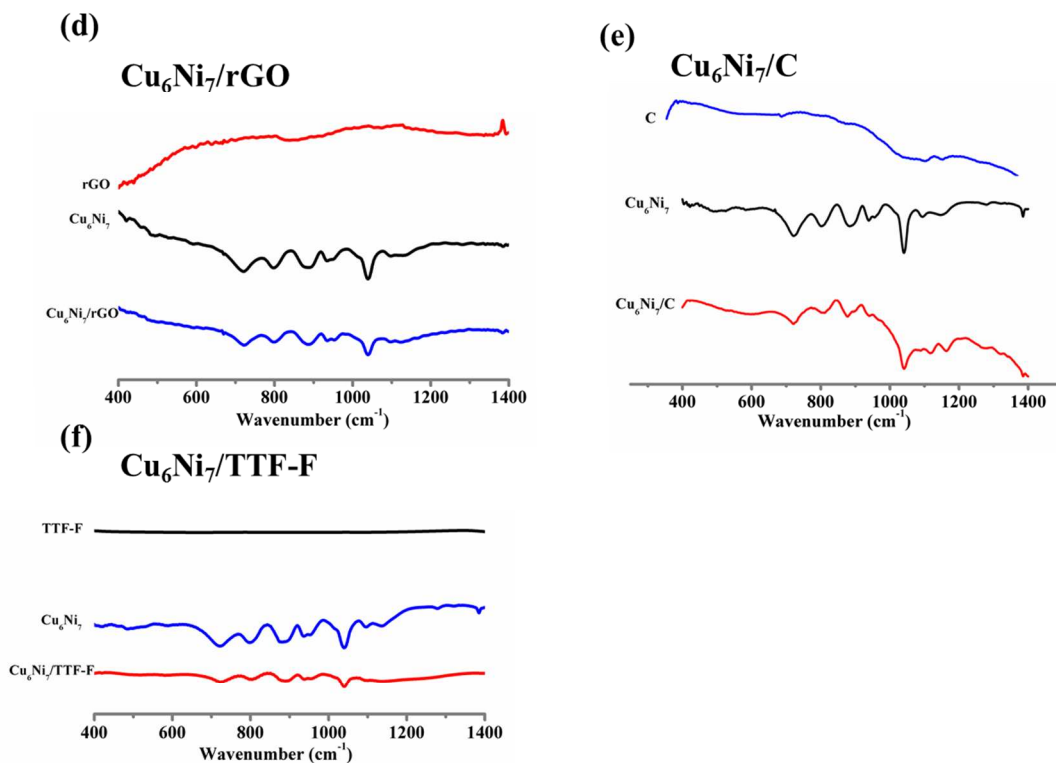


Figure S7. FT-IR spectra of $\text{CuP}_2\text{W}_{18}$ (a), Cu_6Co_7 (b), Cu_6Ni_7 (c), $\text{Cu}_6\text{Ni}_7/\text{rGO}$ (d), $\text{Cu}_6\text{Ni}_7/\text{C}$ (e) and $\text{Cu}_6\text{Ni}_7/\text{TTF-F}$ (f).

Comparing the IR spectra of Cu_6Ni_7 and $\text{Cu}_6\text{Ni}_7/\text{C}$ and $\text{Cu}_6\text{Ni}_7/\text{rGO}$, it is observed that the $\nu_{\text{as(W=O)}}$ (935 cm^{-1} in Cu_6Ni_7 ; 936 cm^{-1} in $\text{Cu}_6\text{Ni}_7/\text{rGO}$; 940 cm^{-1} for $\text{Cu}_6\text{Ni}_7/\text{C}$) and $\nu_{\text{as(W-O-W)}}$ (796 and 882 cm^{-1} in Cu_6Ni_7 ; 798 and 888 cm^{-1} in $\text{Cu}_6\text{Ni}_7/\text{rGO}$; 807 and 890 cm^{-1} in $\text{Cu}_6\text{Ni}_7/\text{C}$) vibrations are blue-shifted in the composite compared to the pure POM compounds.

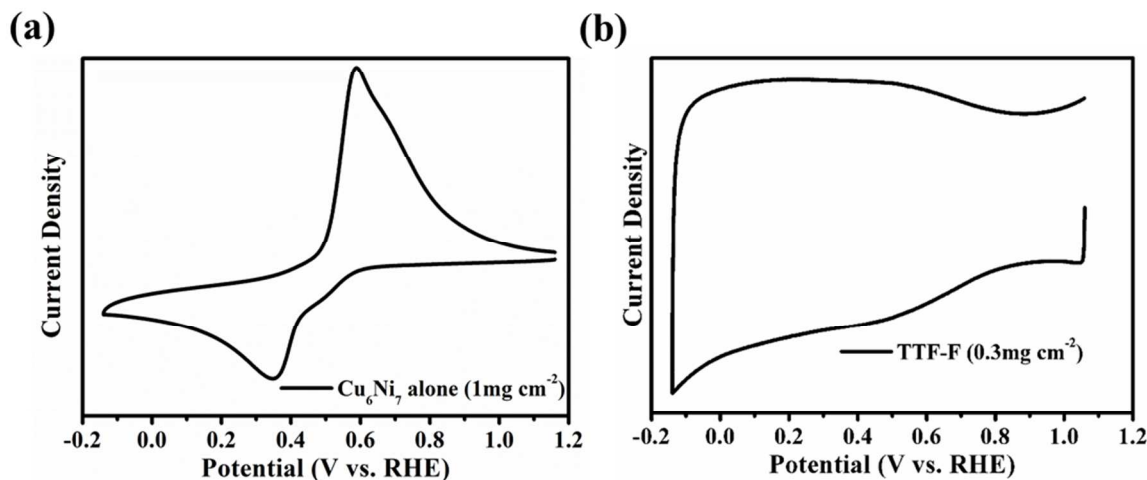


Figure S8. CV curves of Cu_6Ni_7 alone (a) and TTF-F alone (b) in Ar-saturated 0.2 M $\text{NaH}_2\text{PO}_4/\text{NaOH}$ (pH=7.0).

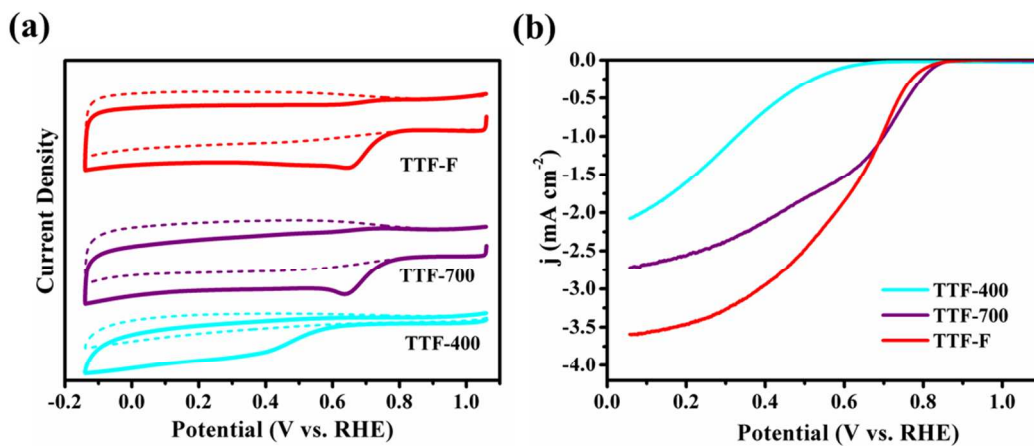


Figure S9. (a) CV curves of TTFs in Ar- (dashed lines) and O_2 -saturated (solid lines) $0.2\text{ M NaH}_2\text{PO}_4/\text{NaOH}$ solution (pH=7.0, scanning rate: 10 mV s^{-1}); (b) LSV curves of TTFs in O_2 -saturated $0.2\text{ M NaH}_2\text{PO}_4/\text{NaOH}$ (pH=7.0, scan rate: 10 mV s^{-1} ; rotation rate: 1600 rpm).

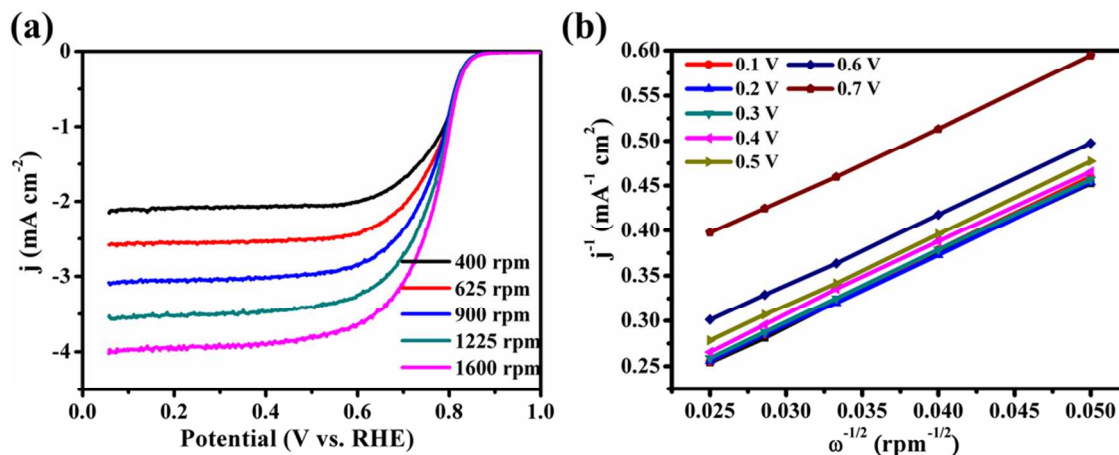


Figure S10. (a) LSV curves of Cu₆Ni₇/TTF-F in O₂ -saturated 0.2 M NaH₂PO₄/NaOH electrolyte (pH = 7.0, scan rate: 10 mV s⁻¹; rotating rate: 400 rpm-1600 rpm); (b) K-L plots calculated from the LSV curves.

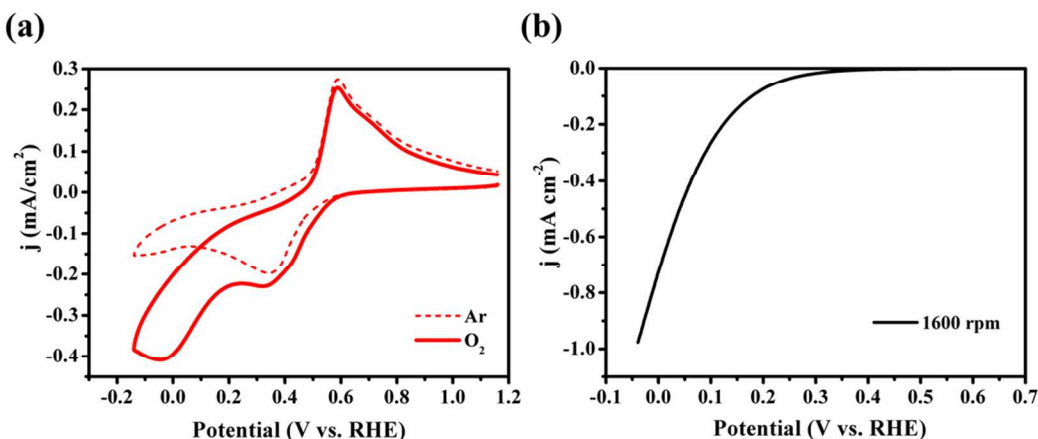


Figure S11. (a) CV curves of Cu₆Ni₇ in Ar- (dashed line) and O₂-saturated (solid lines) 0.2 M NaH₂PO₄/NaOH solution (pH=7.0, scanning rate: 10 mV s⁻¹); (b) LSV curves of Cu₆Ni₇ in O₂-saturated 0.2 M NaH₂PO₄/NaOH (pH=7.0, scan rate: 10 mV s⁻¹; rotation rate: 1600 rpm).

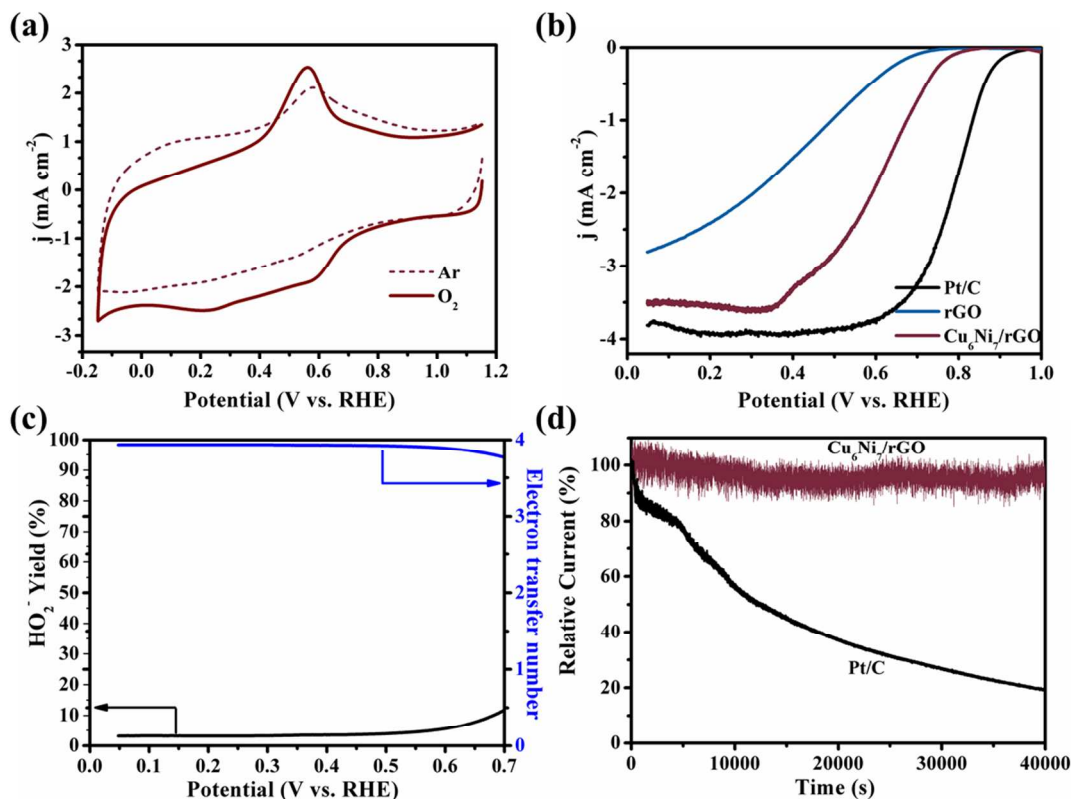


Figure S12. (a) CV curves of $\text{Cu}_6\text{Ni}_7/\text{rGO}$ in Ar- and O_2 -saturated 0.2 M $\text{NaH}_2\text{PO}_4/\text{NaOH}$ (pH=7.0); (b) LSV curves of different catalysts in 0.2 M $\text{NaH}_2\text{PO}_4/\text{NaOH}$; (c) the HO_2^- yield at various disk electrode potential in 0.2 M $\text{NaH}_2\text{PO}_4/\text{NaOH}$; (d) the stability evaluation of $\text{Cu}_6\text{Ni}_7/\text{rGO}$ tested by the current–time chronoamperometric responses at 0.65 V vs. RHE in O_2 -saturated 0.2 M $\text{NaH}_2\text{PO}_4/\text{NaOH}$ solution.

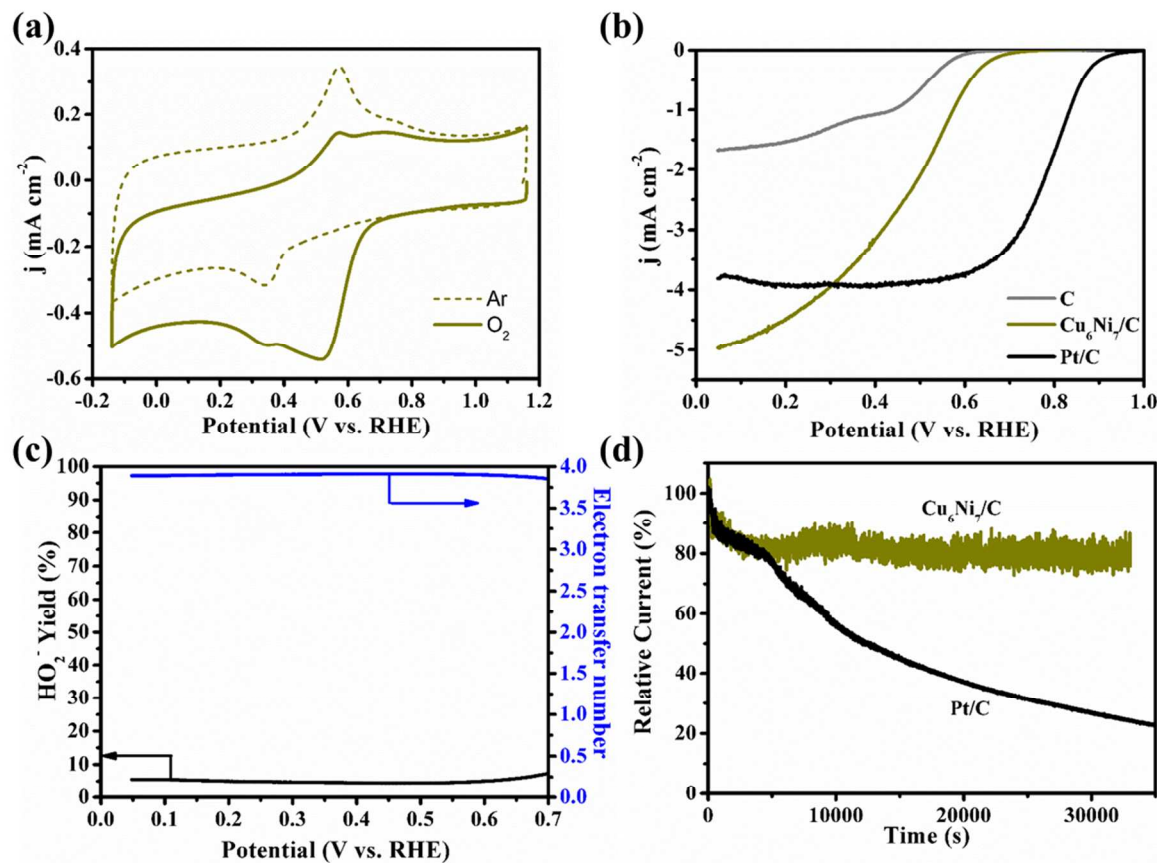


Figure S13. (a) CV curves of $\text{Cu}_6\text{Ni}_7/\text{C}$ in Ar- and O_2 -saturated 0.2 M $\text{NaH}_2\text{PO}_4/\text{NaOH}$ (pH=7.0); (b) LSV curves of different catalysts in 0.2 M $\text{NaH}_2\text{PO}_4/\text{NaOH}$; (c) the HO_2^- yield at various disk electrode potential in 0.2 M $\text{NaH}_2\text{PO}_4/\text{NaOH}$; (d) the stability evaluation of $\text{Cu}_6\text{Ni}_7/\text{C}$ tested by the current-time chronoamperometric responses at 0.65 V vs. RHE in O_2 -saturated 0.2 M $\text{NaH}_2\text{PO}_4/\text{NaOH}$ solution.

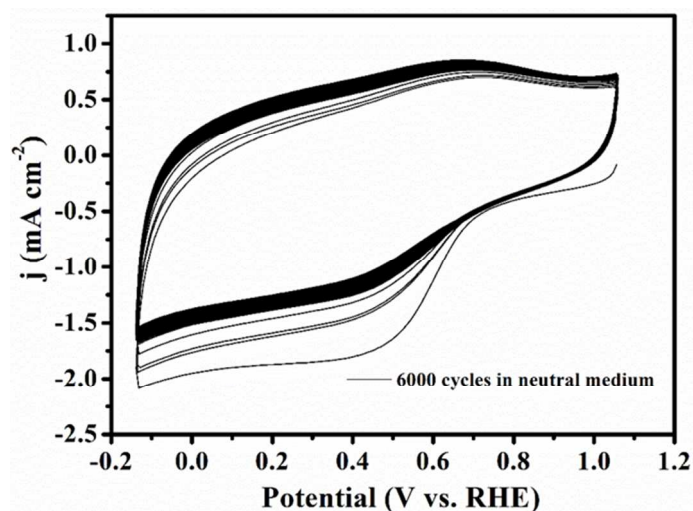


Figure S14. (a) CVs during 6000 cycles in O_2 -saturated 0.2M $\text{NaH}_2\text{PO}_4/\text{NaOH}$ (200 mV s^{-1} for 12000 segments).

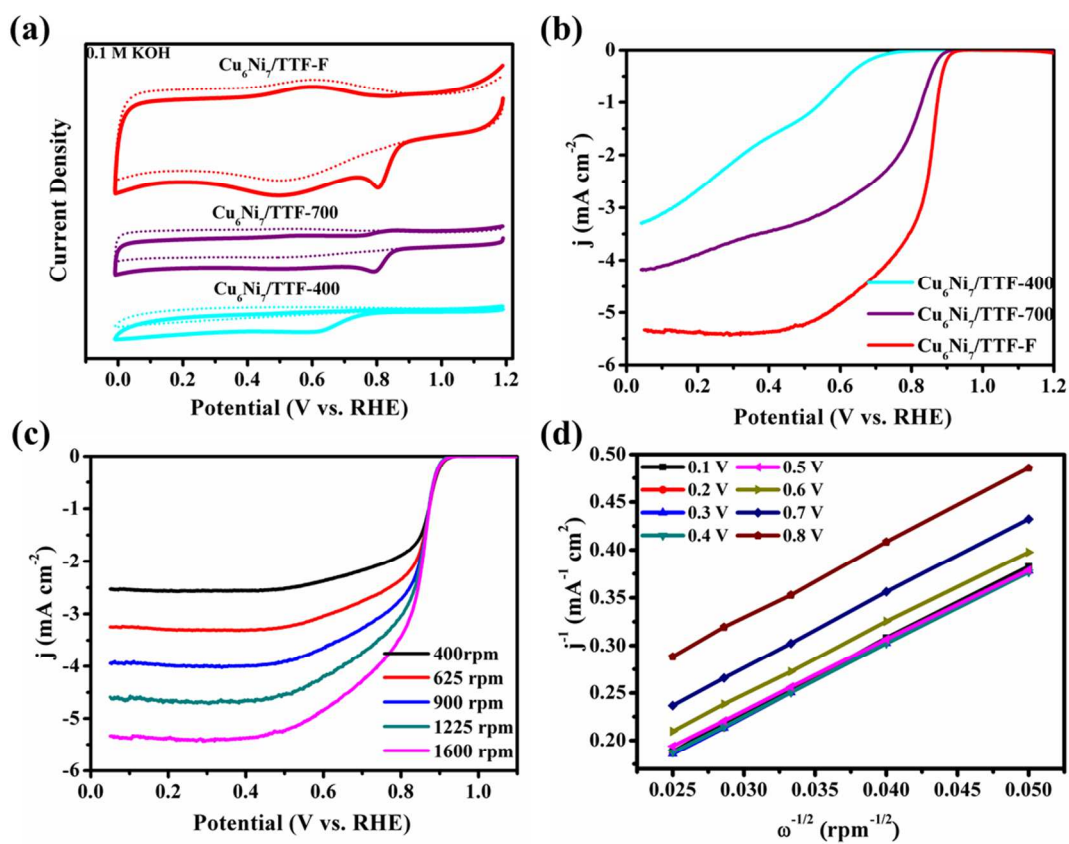


Figure S15. (a) CV curves of Cu₆Ni₇/TTF-F, Cu₆Ni₇/TTF-700 and Cu₆Ni₇/TTF-400 in Ar- (dashed lines) and O₂-saturated (solid lines) 0.1 M KOH; (b) LSV curves of different catalysts in 0.1 M KOH; (c) LSV curves of Cu₆Ni₇/TTF-F in O₂ -saturated 0.1 M KOH electrolyte (scan rate: 10 mV s⁻¹; rotating rate: 400 rpm -1600 rpm); (d) K-L plots calculated from (c).

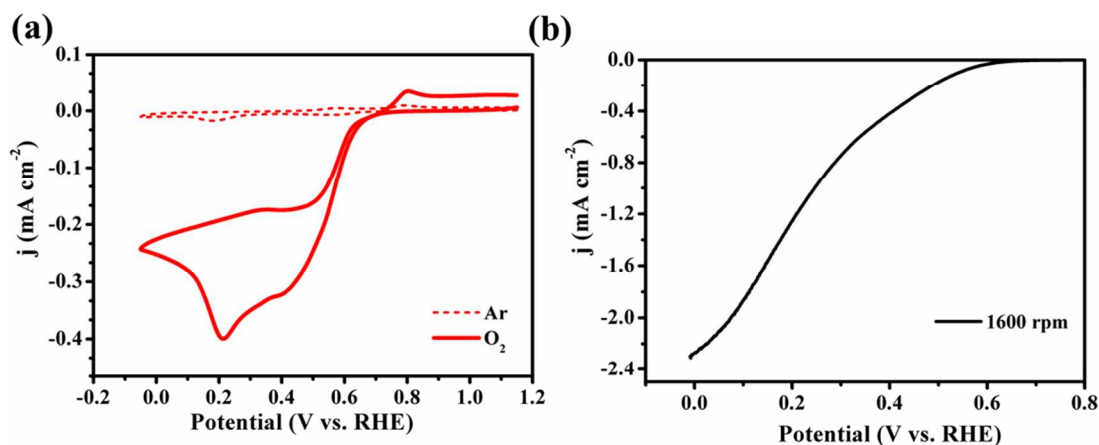


Figure S16. (a) CV curves of Cu₆Ni₇ in Ar- (dashed line) and O₂-saturated (solid line) 0.1 M KOH (scanning rate: 10 mV s⁻¹); (b) LSV curves of Cu₆Ni₇ in O₂-saturated 0.1 M KOH (scan rate: 10 mV s⁻¹; rotation rate: 1600 rpm).

As shown in Figure S16a, the CV pattern of Cu₆Ni₇ obtained in the presence of argon is composed by two reduction waves peaking at +0.58 V and +0.2 V respectively and attributed to the stepwise reduction of Cu^{II} centers into Cu⁰ through Cu^I. Despite of these two waves, CV for Cu₆Ni₇ in O₂ also shows a sharp reduction peaks at 0.2V, attributed to oxygen reduction wave, indicating the POM possesses oxygen reduction activities. The reoxidation of the resulting Cu⁰ in Ar is featured by two spaced waves located at +0.55 and ca. +0.75 V respectively. Different from Ar, reoxidation of Cu⁰ in O₂ is just featured by one big wave at +0.75V. Figure S15a compares the CV characteristics of Cu₆Ni₇/TTF-F observed in the argon- and oxygen-saturated media. In the presence of argon, the broad reduction wave peaking at +0.5 V is a combination of the Cu

centers reduction waves and that of TTF-F. In contrast, the characteristics of both re-oxidation waves of Cu^0 are not obscured by TTF-F. A well-defined peak observed at +0.81 V in the presence of oxygen but not in the argon-saturated electrolyte is attributed to the oxygen reduction peak.

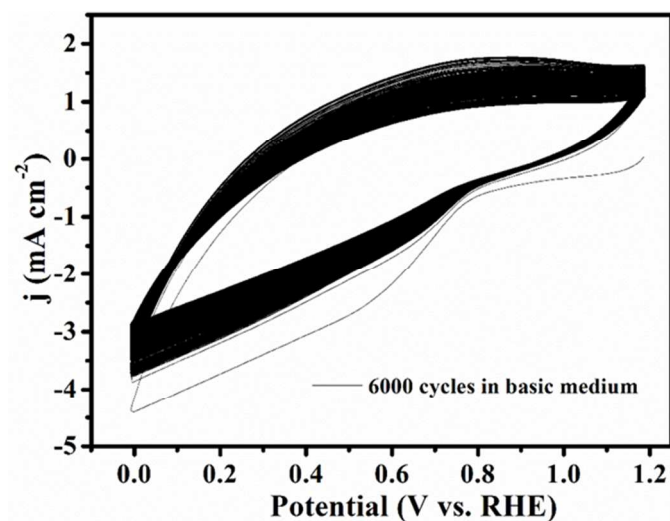


Figure S17. CVs during 6000 cycles in O_2 -saturated 0.1M KOH solution (200 mV s^{-1} for 12000 segments).

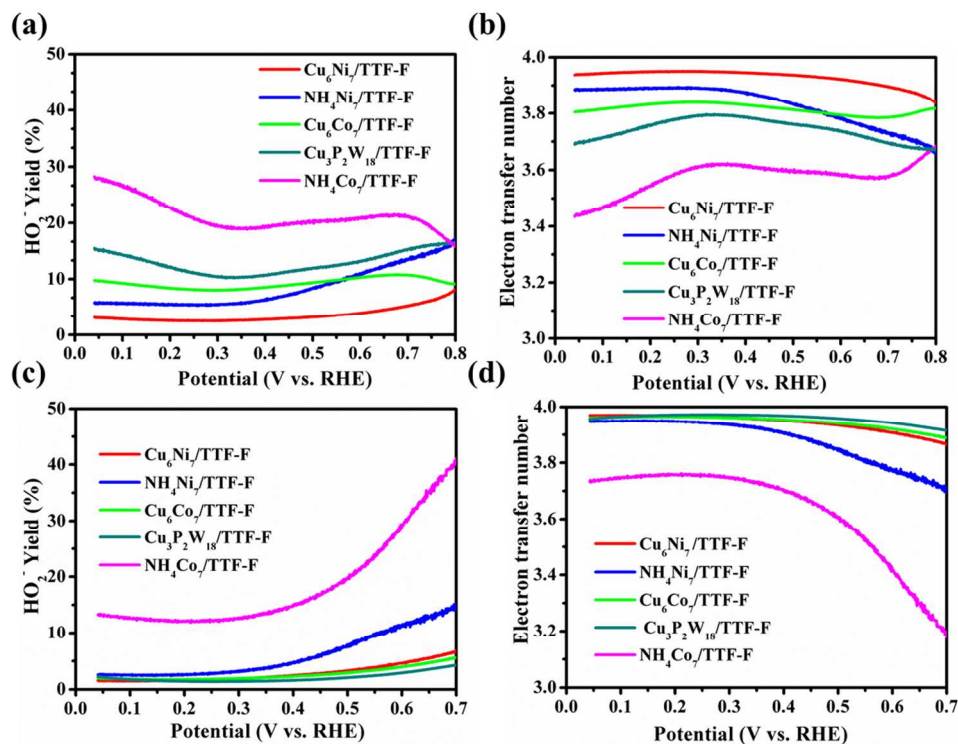


Figure S18. (a) The HO_2^- yield and (b) electron transfer number at various disk electrode potential in 0.1M KOH; (c) the HO_2^- yield and (d) electron transfer number at various disk electrode potential in 0.2 M $\text{NaH}_2\text{PO}_4/\text{NaOH}$.

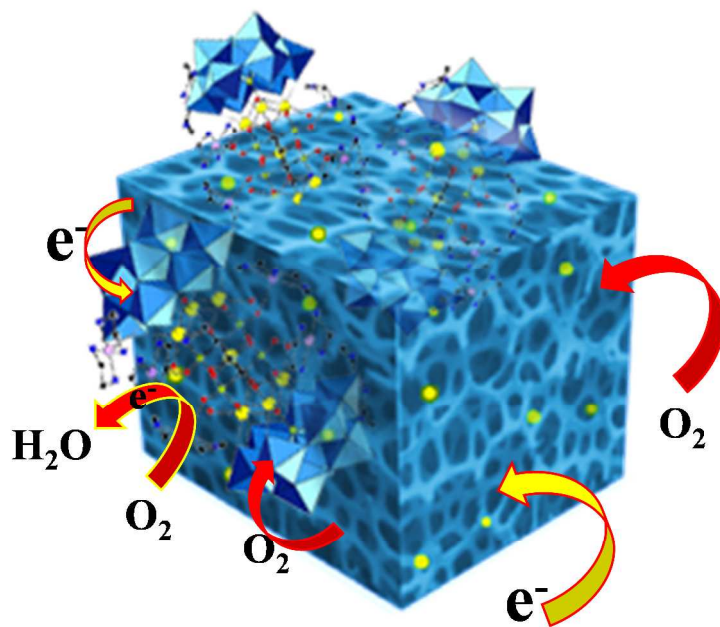


Figure S19. Mechanism of different POM catalyze ORR.

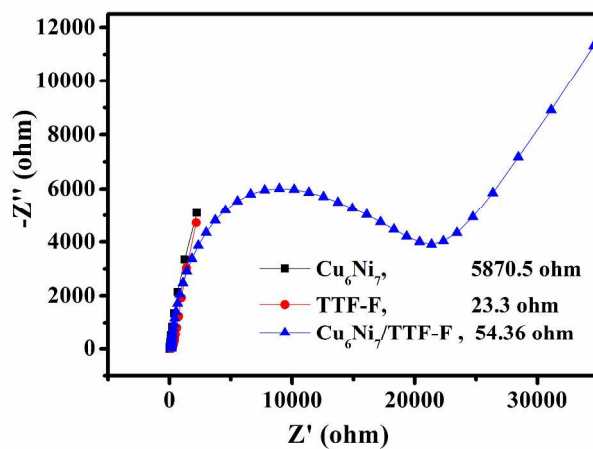


Figure S20. Nyquist plots of Cu_6Ni_7 , TTF-F and $\text{Cu}_6\text{Ni}_7/\text{TTF-F}$. The Nyquist plots reveal that the resistance of TTF-F highly depends on the adsorption of Cu_6Ni_7 . As Cu_6Ni_7 is a poor conductivity, when it combined with TTF-F will even make the resistances of the TTF-F electrodes higher.

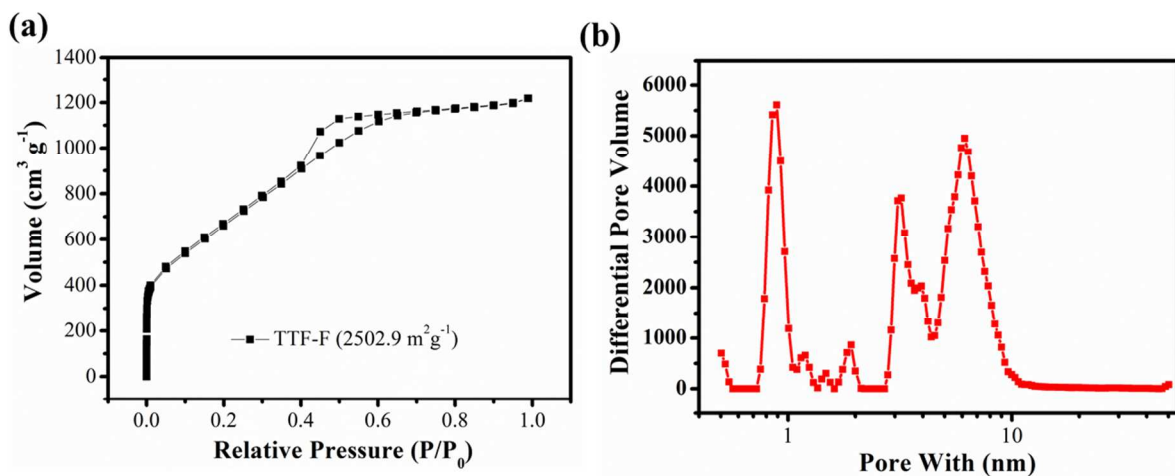


Figure S21. (a) Nitrogen adsorption–desorption isotherms of TTF-F. (b) Pore size distributions of TTF-F.

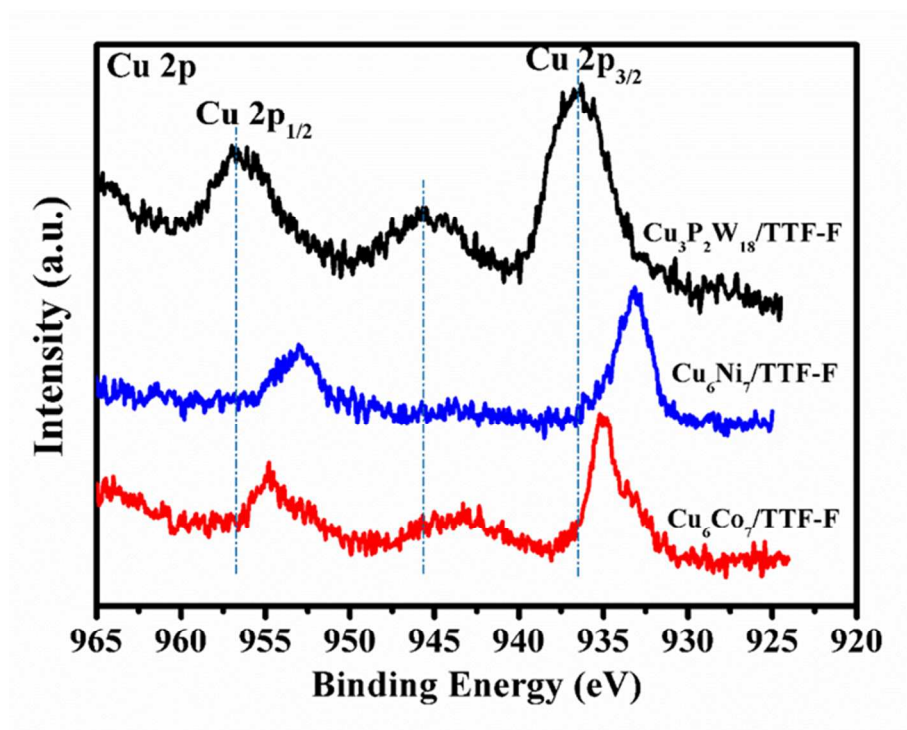


Figure S22. XPS spectra of Cu 2p of $\text{Cu}_3\text{P}_2\text{W}_{18}/\text{TTF-F}$, $\text{Cu}_6\text{Ni}_7/\text{TTF-F}$, $\text{Cu}_6\text{Co}_7/\text{TTF-F}$.

Table S2. Summary of ORR catalytic activities of catalysts in basic medium.

Catalysts	E_{onset} (V vs. RHE)	I_L (mA/cm ²)	HO_2^- 0.05V/0.6V	n 0.05V/0.6V	O_2 reduction wave potential (V vs. RHE)
$\text{Cu}_6\text{Ni}_7/\text{TTF-F}$	0.906	5.33	3.1/3.9	3.94/3.92	0.806
$\text{Cu}_6\text{Ni}_7/\text{TTF-700}$	0.883	4.17	25.4/20.6	3.49/3.59	0.790
$\text{Cu}_6\text{Ni}_7/\text{TTF-400}$	0.714	3.29	30.4/68.5	3.39/2.63	0.565
TTF-F	0.853	4.57	13.3/33.7	3.73/3.32	0.754
TTF-700	0.854	3.30	37.4/43.5	3.25/3.13	0.753
TTF-400	0.724	2.66	49.1/63.9	3.02/2.72	0.601
$\text{Cu}_6\text{Ni}_7/\text{rGO}$	0.930	4.97	7.8/13.7	3.93/3.72	0.790
$\text{Cu}_6\text{Ni}_7/\text{C}$	0.880	4.05	4.6/15.4	3.91/3.69	0.770
$\text{NH}_4\text{Ni}_7/\text{TTF-F}$	0.873	4.76	5.6/12.3	3.88/3.75	0.758
$\text{Cu}_6\text{Co}_7/\text{TTF-F}$	0.897	5.29	9.2/10.7	3.81/3.78	0.802
$\text{Cu}_3\text{P}_2\text{W}_{18}/\text{TTF-F}$	0.892	4.75	14.2/14.12	3.71/3.72	0.797
$\text{NH}_4\text{Co}_7/\text{TTF-F}$	0.902	4.47	26.5/21.4	3.47/3.57	0.796
Pt/C	0.960	5.38	3.1/4.5	3.93/3.91	0.820

Table S3. Summary of surface areas and Pore size of different carbon support. For TTF-400, TTF-700 and TTF-F, the results come from nitrogen adsorption/desorption measurement. The rGO^{13-15} and Vulcan carbon XC-72¹⁶ results come from references.

Catalysts	BET surface areas (m ² g ⁻¹)	Pore Volume (cm ³ g ⁻¹)	Average pore size (nm)
TTF-400	1175	0.66	2.2
TTF-700	2237	1.65	2.97
TTF-F	2503	1.88	3.0
rGO	<2000	\	\
Vulcan carbon XC-72	228	0.4	<0.2

Computational Calculation Section:

Models and Method:

Simplified molecular structures of Co-Cu-H and Ni-Cu-H ligands were derived from XRD characterizations. For each structure, the B3LYP/6-311++g** computational model (with reasonable accuracy and reasonable cost) was employed for C, O, N, P and H atom and B3LYP/lanl2dz basis set was employed for Cu, Co and Ni atoms to study all of the structures and NBO (natural bond orbital) charges. There is no imaginary frequency for all of the structures which promises a local minimum. All of the calculations were performed using the Gaussian 09 suite of programs. To show the structure clearly, all H atoms were not presented in the charge distribution.

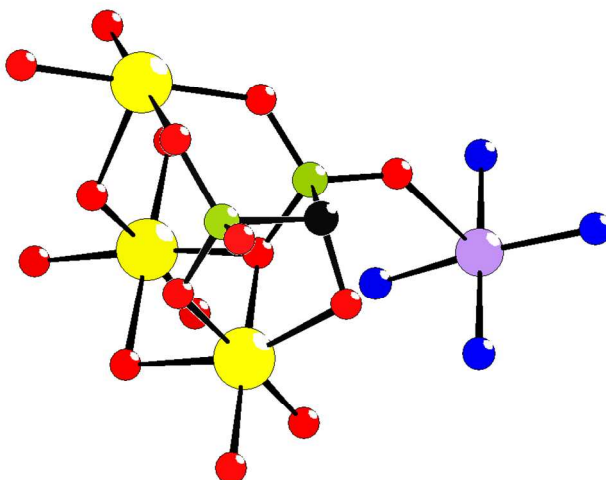


Figure S23. Structure fragment of Cu_6Ni_7 or Cu_6Co_7 for DFT calculation.

Reference

- (1) Hao, L.; Zhang, S.; Liu, R.; Ning, J.; Zhang, G.; Zhi, L. Bottom-Up Construction of Triazine-Based Frameworks as Metal-Free Electrocatalysts for Oxygen Reduction Reaction. *Adv. Mater.* **2015**, 27, 3189-3195.

- (2) Wang, J.; Gao, Z.; Li, Z.; Wang, B.; Yan Y.; Liu Q.; Mann T.; Zhang M.; Jiang Z. Green Synthesis of Graphene Nanosheets/ZnO Composites and Electrochemical Properties. *J. Solid State Chem.* **2011**, *184*, 1421-1427.
- (3) Sheldrick, G. M. SADABS, Program for Scaling and Correction of Area Detector Data, University of Göttingen, Germany, 1997.
- (4) Blessing, R. H. An Empirical Correction for Absorption Anisotropy. *Acta Crystallogr.* **1995**, *A51*, 33-38.
- (5) Sheldrick, G. M. SHELX-TL, Software Package for the Crystal Structure Determination, Siemens Analytical X-ray Instrument Division, Madison, WI USA, 1994.
- (6) Wen, Z.; Ci, S.; Zhang, F.; Feng, X.; Cui, S.; Mao, S.; Luo, S.; He, Z.; Chen, J. Nitrogen-Enriched Core-Shell Structured Fe/Fe₃C-C Nanorods as Advanced Electrocatalysts for Oxygen Reduction Reaction. *Adv. Mater.* **2012**, *24*, 1399-1404.
- (7) Zhao, Y.; Watanabe, K.; Hashimoto, K. Self-Supporting Oxygen Reduction Electrocatalysts Made from a Nitrogen-Rich Network Polymer. *J. Am. Chem. Soc.* **2012**, *134*, 19528-19531.
- (8) Iwase, K.; Yoshioka, T.; Nakanishi, S.; Hashimoto, K.; Kamiya, K. Copper-Modified Covalent Triazine Frameworks as Non-Noble-Metal Electrocatalysts for Oxygen Reduction. *Angew. Chem. Int. Ed.* **2015**, *54*, 11068-11072.
- (9) Zhang, B.; Wen, Z.; Ci, S.; Mao, S.; Chen, J.; He, Z. Synthesizing Nitrogen-Doped Activated Carbon and Probing its Active Sites for Oxygen Reduction Reaction in Microbial Fuel Cells *ACS Appl. Mater. Interfaces* **2014**, *6*, 7464-7470.

- (10) Tang, H.; Cai, S.; Xie, S.; Wang, Z.; Tong, Y.; Pan, M.; Lu, X. Metal–Organic-Framework-Derived Dual Metal- and Nitrogen-Doped Carbon as Efficient and Robust Oxygen Reduction Reaction Catalysts for Microbial Fuel Cells. *Adv. Sci.* **2016**, *3*, 1500265.
- (11) Watson, V. J.; Delgado, C. Nieto; Logan, B. E. Influence of Chemical and Physical Properties of Activated Carbon Powders on Oxygen Reduction and Microbial Fuel Cell Performance. *Environ. Sci. Technol.* **2013**, *47*, 6704-6710.
- (12) Rappé, A. K.; Goddard III, W. A. Charge Equilibration for Molecular Dynamics Simulations *J. Phys. Chem.* **1991**, *95*, 3358-3363.
- (13) Stoller, M.; Park, S.; Zhu, Y.; An, J.; Ruoff, R. Graphene-Based Ultracapacitors. *Nano Lett.* **2008**, *8*, 3498–3502.
- (14) Si, Y.; Samulski, E. Exfoliated Graphene Separated by Platinum Nanoparticles. *Chem. Mater.* **2008**, *20*, 6792–6797.
- (15) Schniepp, H.; Li, J.; McAllister, M.; Sai, H.; Herrera-Alonso, M.; Adamson, D.; Prud'homme, R.; Car, R.; Saville, D.; Aksay, I. Functionalized Single Graphene Sheets Derived from Splitting Graphite Oxide. *J. Phys. Chem. B* **2006**, *110*, 8535–8539.
- (16) Soboleva, T.; Zhao, X.; Malek, K.; Xie, Z.; Navessin, T.; Holdcroft, S. On the Micro-, Meso-, and Macroporous Structures of Polymer Electrolyte Membrane Fuel Cell Catalyst Layers. *ACS Appl. Mater. Interfaces* **2010**, *2*, 375–384.